Scholars' Mine

Masters Theses   Student Theses and Dissertations

Spring 2012

Optical coherence tomography for biomedical imaging

Edward Henry Pienkowski

OPTICAL COHERENCE TOMOGRAPHY

FOR BIOMEDICAL IMAGING

by

EDWARD HENRY PIENKOWSKI JR

A THESIS

Presented to the Faculty of the Graduate School of the

MISSOURI UNIVERSITY OF SCIENCE AND TECHNOLOGY

In Partial Fulfillment of the Requirements for the Degree

MASTER OF SCIENCE IN ELECTRICAL ENGINEERING

2012

Approved by

Dr. Hai Xiao, Advisor
Dr. J. Greg Story
Dr. Randy H. Moss

ABSTRACT

Two projects are presented in this thesis; 1) a hollow core, concentrically symmetric beam splitting Michelson interferometric probe for optical coherence tomography and 2) the imaging of bioactive ceramic scaffolds using swept source optical coherence tomography.

The key component of the interferometer is a compact, small diameter probe composed of a collimating lens, hollow core beam splitting tube, and a focusing lens intended to be used for endoscopic imaging. The beam splitting tube was created by sputter coating the distal endface of a finely polished thick wall capillary tube with a highly reflective gold layer. Part of the light travels through the wall of the tube is reflected by the distal endface, forming a reference arm, and part passes through the hollow core to be backscattered by the sample material, forming a sample arm. To demonstrate the functionality of the probe, cross-sectional and volumetric images of a simple sample were obtained. An additional advantage of this probe is an easily adjustable working distance.

Bioactive ceramic scaffolds have been shown to possess high degrees of conversion to hydroyapatite and are currently used in a variety of biomedical applications. In an effort to enhance current research and demonstrate the feasibility of optical coherence tomography as a bioceramic imaging modality, a swept source optical coherence tomography system was employed in the imaging of a variety of ceramic bioscaffolds. In order to demonstrate the imaging capabilities of an optical coherence tomography system for imaging of ceramic bioscaffolds, images of scaffolds were compared to other imaging modalities.

ACKNOWLEDGMENTS

TABLE OF CONTENTS

LIST OF ILLUSTRATIONS

LIST OF TABLES

NOMENCLATURE

Symbol	Description
U	Wave
A	Amplitude
k	Wave Number
r	Radial Distance
ω	Angular Frequency
t	Time
Φ	Phase Shift
θ	Angular Difference Between Polarizations

1. INTRODUCTION

1.1. BACKGROUND

The development of the microscope allowed Robert Hooke to first discover biological cells within a piece of cork in 1665. Over three centuries later, optical microscopes are still in use in biological analysis and medical diagnostics, yet modern science has developed additional diagnostic techniques for medical use, each possessing various advantages and disadvantages for specific applications. A number of the more recently developed imaging techniques employed in medical facilities, such as x-ray computed tomography, are tomographic in nature. These tomographic techniques take advantage of the various properties of biological tissue to produce images with varying degrees of resolution, contrast, and penetration depth. However, the medical community is continually searching for techniques that do not involve invasive procedures, radioactive isotopes, or ionizing radiation [1], [2].

One of the more recent tomographic imaging techniques that has been developed is optical coherence tomography (OCT) which was first demonstrated in 1991 [3]. OCT is an optical analog to ultrasound, in which the reflections of ultrasonic waves are used to produce images, yet the higher frequency of light allows for resolutions that are generally over an order of magnitude higher than those of ultrasound [1], [2]. OCT is a non-invasive, high-resolution, interferometric imaging modality that employs non-ionizing light for imaging. Through the use of optical interferometry, OCT is able to produce cross-sectional images of biological tissue with resolutions on the order of approximately ten microns. However, unlike ultrasound, OCT imaging can be done in a non-contact manner [4].

1.2. OBJECTIVES

Optical coherence tomography has been shown to be of notable use in ophthalmology and dermatology. The properties of OCT lend to the utility of the technology for diagnosing various conditions in these fields; OCT is a non-invasive, non-

contact imaging modality that is able to produce high-resolution, cross-sectional, subsurface, morphological tissue images without the use of damaging ionizing radiation, radioisotopes, or ultraviolet radiation [2], [4]. As such, non-contact diagnostic imaging of the cornea and retina can be achieved without risk of eye damage or the need for a tissue biopsy [5], [6]; the situation is similar for skin lesion assessment [1], [7]. Following the success of OCT in these fields, a notable amount of interest has risen for OCT systems that are able to image internal organs and structures as well. When employed in a minimally invasive endoscopic probe, OCT offers improved resolution over other endoscopic imaging techniques, including intravascular ultrasound (IVUS) and rod-lens endoscopy.

In addition to the investigation of endoscopic OCT devices, there is also interest in expanding the variety of OCT application areas, including the investigation of the possible application of OCT to imaging of implanted bioceramic scaffolds and wound healing.

Since the initial development of 45S5 bioactive glass by Hench et al. in 1971 [8], bioactive glasses have been shown to possess a notable ability to bond to various tissues and to supplement the growth of bone cells during repair [9], [10], [11]. As such, bioactive glasses have become a fast growing medical utility for applications such as orthopedic implant coatings, dental implants, bone fillers, drug delivery, and tissue engineering scaffolds, with various formulations currently in use and development [12].

A number of techniques are involved in the assessment of the properties, such as porosity and hydroyapetite conversion, of these bioactive glasses, including X-ray microtomography, electron microscopy, and histological sectioning. Histological sectioning and electron microscopy are both able to provide images with high degrees of both resolution and contrast. Yet, both histological sectioning and electron microscopy require sacrificing test animals and performing tissue biopsy in humans for imaging purposes, preventing in situ imaging. Thus, these techniques require sacrificial samples or invasive biopsy to fully assess material properties and changes that occur over time when compared to in situ techniques [12], [13], [14].

Sharing some similarities with X-ray microtomography, OCT is a nondestructive, high-resolution, interferometric imaging modality that is well suited for in situ

applications [1], [12]. As it is currently employed in many biological applications, OCT is capable of penetrating up to approximately 4mm of soft tissue to produce cross-sectional and volumetric morphological images with micrometer resolution [12]. It is able to produce tomographic images with significantly higher resolution than other modern imaging modalities, including X-ray, ultrasound, MRI, and PET [15]. However, it does so without requiring the use of ionizing radiation or radioactive isotopes, which is of particular interest when performing in vivo imaging.

A number of chronic medical conditions can impair the wound healing ability of the human body, including limited mobility which can result in bed sores and diabetes which can often result in non-healing ulcers. It is not uncommon for these non-healing wounds to result in the loss of limbs and/or life. In an effort to help alleviate these conditions and induce proper wound healing, innovative medical products and procedures are regularly investigated [16], [17]. However, it is often inconvenient to analyze the morphological structure of the wound healing process because the analysis requires an invasive tissue biopsy. Yet, because of its non-invasive properties, OCT is particularly suited to analyze the wound healing process, as previously described.

1.3. THEORY

1.3.1. Plane Wave Interference. A plane wave is a wave with a constant wavelength composition that has infinite planar wavefronts which travel with a regular sinusoidal variation. In reality, plane waves do not exist due to the requirement that the plane of the wave must extend infinitely in all radial directions. However, relatively accurate approximations can be created, particularly when the propagation distance is significantly higher than the wavelength of the wave itself, which is common in high frequency waves, such as is the case with light waves. The general and complex exponential forms of plane waves (using a radial coordinate system) are given in **Equation 1.1** and **Equation 1.2**, respectively.

$$U(r,t) = A\cos(kr - \omega t + \phi)$$
[**Equation 1.1**]

$$U(r,t) = Ae^{i(kr - \omega t + \phi)}$$
[**Equation 1.2**]

where U is the wave, A is the amplitude of the wave, k is the wave number, r is the radial distance, ω is the angular frequency, t is time, and Φ is the phase shift of the wave.

Interference occurs when two or more waves are propagating in the same space. The components of the waves that are polarized in the same or opposing directions interact to form a composite wave that is the result of the superposition of the components. The resulting wave can possess an amplitude that is greater than the amplitude of either precursor wave in a process known as constructive interference or, conversely, it can produce a wave that is of lesser amplitude than either of the precursor waves in a process known as destructive interference.

However, for two waves to interfere, they must be coherent, that is they must possess nearly the same wavelength and their polarizations must not be orthogonal. Though, waves with differing polarizations can be partially coherent, where the interference is not complete but still present, as would be the case if two waves of the same wavelength possessed polarizations that were not parallel, but neither were they orthogonal. This can be seen by considering **Equation 1.3**, which is the addition of two coherent waves of differing amplitudes,

$$U(r,t) = A_1 e^{(ikr) \cdot u} + A_2 e^{(ikr) \cdot u}$$

[**Equation 1.3**]

where A_1 is the amplitude of the first wave and A_2 is the amplitude of the second wave, and both waves possess the same wavelength and phase.

The intensity of the superposed wave is then shown in **Equation 1.4**;

$$I(r,t) = A_1^2 + A_2^2 + 2 A_1 A_2 \cos[k(r_2 - r_1) \cdot u]$$

[**Equation 1.4**]

where the first term is the square of the amplitude of the first wave, the second term is the square of the amplitude of the second wave, and the third term is the sinusoidally varying result of the superposition of the amplitudes of the two waves. The sinusoidal term is what is commonly known as the interferogram of the wave. In addition, the (r_2-r_1) term can be more succinctly denoted as θ, which is the angular difference between the polarizations of the two interfering waves [18], [19].

1.3.2. Interferometers. Often the method used to produce coherent waves for interference purposes it to split the light from a single source into two or more separate waves, through the use of a beam splitter, which are then able to interfere.

1.3.2.1. Michelson. The Michaelson interferometer is the most straightforward and most commonly used interferometer in interferometric systems [20], [21]. **Figure 1.1** is an illustration of a Michaelson interferometer where a beam splitter separates the incident light into two seaparte beams that travel in orthogonal directions, reflect off mirrors, and then are recombined by the beam splitter to form an interference wave. The two separate paths of the waves are generally referred to as the reference and sample arms of the system. The reference arm employs a simple stationary mirror for reference purposes of the back-reflected wave. The sample arm, however, contains a variable that the system intends to measure through the interference signal.
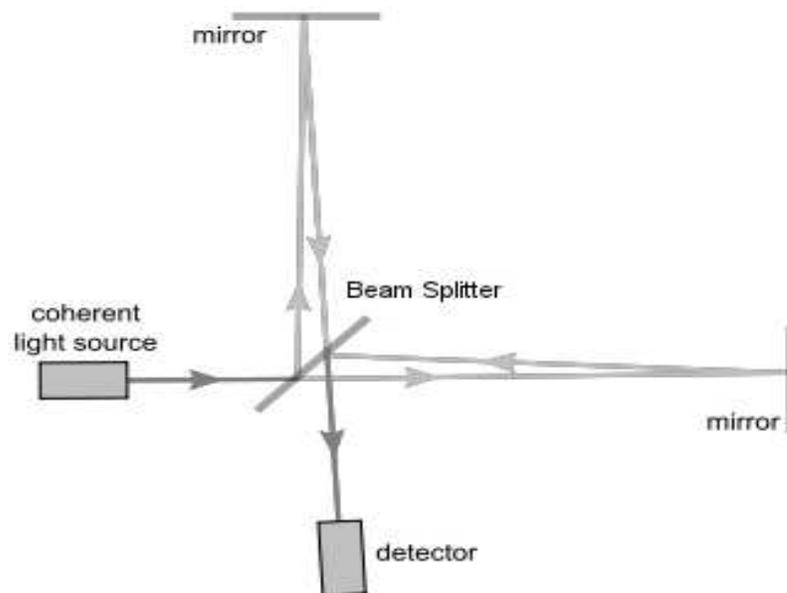
Figure 1.1 Michaelson Interferometer

A beam splitter divides the light source into sample and reference arms, which are reflected by the mirrors and combined by the beam splitter, before reaching the detector.

In an optical system, the interference signal is generally recorded by a photodetector or optical spectrum analyzer, digitized, and then processed by a computer system for various purposes; in the case of OCT, the interference signal will be processed to produce an image of the structure that was measued using the sample arm of the system.

1.3.2.2. Mach-Zehnder. The Mach-Zhender interferometer is another commonly used interferometric configuration. As shown in **Figure 1.2**, a typical Mach-Zehnder interferometer is in principle very similar to the previously described Michaelson interferometer, specifically, the Michaelson Interferometer is a Mach-Zhender Interferometer that has been folded in half, so that only one of the exiting interferograms propagates to the detector (except in fiber optic cases in which a circulator is employed) [21].

Figure 1.2 Mach-Zehnder Interferometer

*A beam splitter divides the light source into sample and reference arms,
which are reflected by the mirrors toward a second beam splitter where
they are combined before reaching the detector.*

However, instead of employing mirrors to reflect the sample and reference beams back toward the original beam splitter for superposition and subsequent detection, the mirrors are angled to reflect the beams toward a second beam splitter that will then combine the beams and send 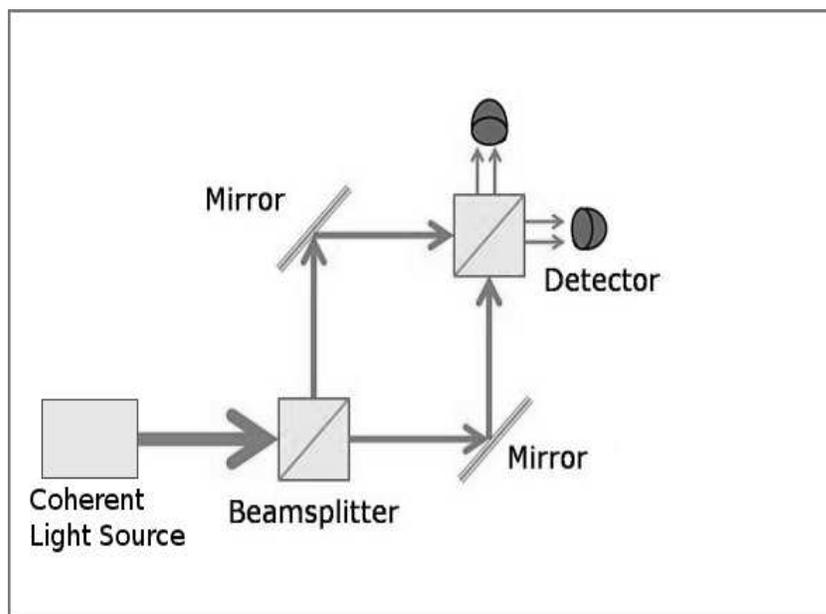the resulting signals to detectors. Because both of the resulting interference signals are able to be detected, the Mach-Zehnder interferometer exhibits greater power efficiency than the Michaelson interferometer. In addition, the Mach-Zehnder interferometer possesses the advantage of the system being generally ready for implementation of balanced detection because the two outputs of the second beam splitter are exactly 180 degrees out of phase with each other and can readily be combined to cancel the common components, leaving only the interferometic comonents [21].

1.3.3. Lasers. The light source employed in OCT is generally some form of coherent light source, commonly a laser. **Figure 1.3** shows a diagram of a generic laser which illustrates the major components of a laser. Two mirrors, one highly reflective and one somewhat less reflective form an optical resonance cavity with a separation that is some multiple of the desired output wavelength divided by two. The pump source introduces energy into the gain medium in order to excite atoms to induce population inversion. Population inversion occurs once the number of excited particles exceeds the number of particles in the ground state, at which time stimulated emission can take place and a laser beam can form [22].

1.3.3.1. Continuous Wave Lasers. One type of laser employed in OCT applications is the continuous wave laser. A continuous wave laser is a laser in which the output power can be considered relatively constant over a significant period of time. While these lasers may be considered to possess a constant power, in reality, most do possess slight amplitude variations due to the presence of multiple lasing modes and variations within the devices due to environmental concerns such as vibration and heat dissipation. However, the time averaged power is fairly consistent over longer periods of time (i.e. seconds or longer) [22].

Continuous wave lasers possess the specific requirement that the population inversion of the gain medium be consistently elevated. As such, the population excited within the gain medium by the pump source of the laser must exceed the population that

decays to produce the output beam. Yet, for many gain media configurations, this is not a possibility due to extremely high pump rate requirements and/or insufficient cooling ability. In such media where continuous wave generation is not a possibility, pulsed lasing may still be possible [22].
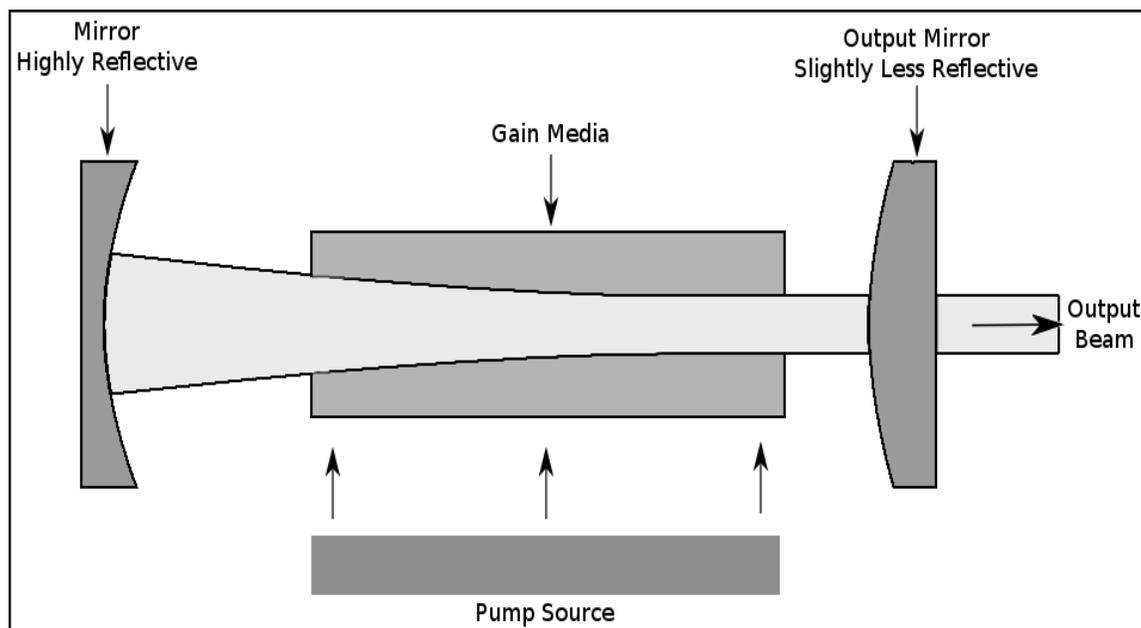
Figure 1.3 General Laser Configuration
A laser consists of a resonant cavity, gain media, and pump source.

1.3.3.2. Pulsed Lasers. Pulsed lasers are those lasers that are not configured to function as continuous wave devices. In pulsed lasing, the output amplitude varies with some time interval, though the time interval may or may not be fixed. A variety of methods can be employed to induce pulsed lasing, including Q-switching and pump pulsing [22].

Q-switching disrupts the quality factor of the resonance cavity within the laser, resulting in an increased buildup of particles in the excited state; once population inversion is achieved, the Q-switch can be turned off (or may be turned off automatically), allowing the cavity to become resonant, inducing laser activation. Through Q-switching, intense pulses of extremely short duration, picoseconds and femtoseconds, can be achieved. There are two general methods used for Q-switching, passive and active. An additional laser element, commonly a saturable absorber, which selectively allows specific wavelengths to propagate and undergo amplification without outside activation can be employed in a *passive q-switching* scheme. If external activation of the pulses is desired, *active q-switching* can be induced inserting an acousto-optic or electro-optic modulator within the laser cavity which reestablishes the resonance within the cavity and allows the excited light to exit the cavity when the modulator is deactivated [22].

Pump pulsing is an active method for inducing pulsed lasing in a laser system that would normally function as a continuous wave device. In these configurations, the pump source is pulsed to raise or lower the population inversion of the system in relation to the lasing threshold, thus inducing non-continuous lasing. However, these devices generally possess significantly longer pulse durations than those of Q-switched lasers [22].

1.3.3.3. Diodes. Laser diodes are semiconductor devices which produce narrowband light emission through the electrical excitation of p-n junctioned band-gap materials with energies in the optical range. In practice, laser diodes are very similar to common LEDs, however, they have been polished to a highly reflective finish, rather than the rounded epoxy packaging commonly surrounding an LED, in order to produce a laser cavity [23], [24].

In addition to traditional laser sources and laser diodes, superluminescent diodes (SLEDs or SLDs) are often employed as light sources. SLDs are didoes which generate amplified spontaneous emission with a relatively wide bandwidth, however, not quite as wide as a general LED. The output power of these devices is significantly higher than that of an LED and is generally in the same range as that of a laser diode. Due to the broader bandwidth of the output, the coherence length of the light is significantly less than that of a laser [25].

1.3.3.4. Swept Source Lasers. Swept source lasers produce a series of narrowband light emissions with sinusoidal frequency variations about a central wavelength. The output wavelength of swept lasers is often fairly broad (~100nm). This variation can be achieved through introducing a sinusoidally varying optical filter to a device that already outputs a fairly broadband signal [26].

1.4. OPTICAL COHERENCE TOMOGRAPHY

As an advancement upon low coherence reflectometry, the original OCT system proposed in by Huang et al. in 1991 [3] employed a Michelson Interferometer in a fiber based system. This device (shown in **Figure 1.4**) split light from a coherent source into sample and reference arms, which was reflected by the sample and a mirror, respectively. The mirror of the reference arm was mounted so that it could be moved longitudinally in order to scan the sample, while at the same time, the sample arm was mounted so that it could scan the sample laterally.
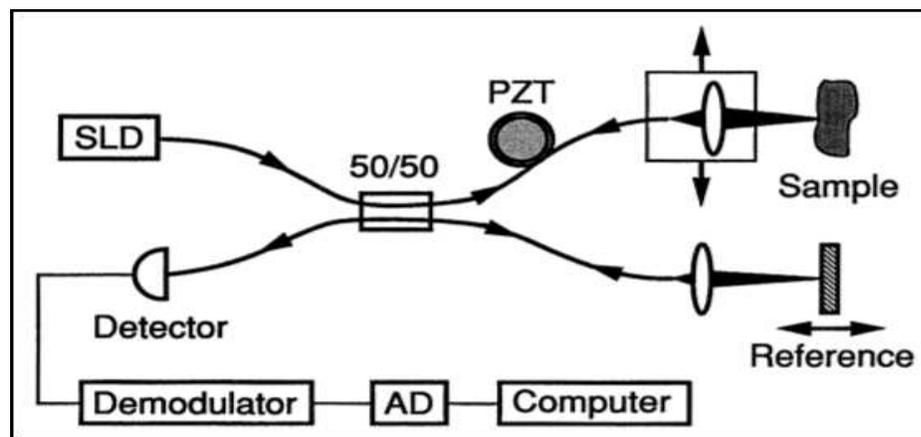
Figure 1.4 Michelson OCT System Diagram

From Huang et al's 1991 article in Science, this Michaelson based OCT system employs a 50/50 beam splitter in a fiber optic system, in which the reference arm is mounted on a translation stage for longitudinal scanning and the sample arm is used for lateral scanning.

A piezoelectric transducer was included in the sample arm in order to produce a phase modulation within the interferometric signal to aid in demodulation and image reconstruction [3]. The scanning performed by this system was named in agreement with previously existing tomographic imaging systems; an <u>A-Scan</u> is a one dimensional profile that provides information on the changes within the depth of the sample; a <u>B-Scan</u> is a two dimensional image that is the result of a combining a linear array of A-Scans to form a two dimensional depthwise image. Multiple B-Scans can also be combined to form a three-dimensional map of a sample. It is important to note that the depth resolution at which the system can scan is limited by the coherence of the source within the sample material and the lateral resolution is limited by the beam waist in the sample [27].

1.4.1. Time Domain OCT. In Time Domain OCT (TDOCT) the path length of the reference arm varies with respect to the pathlength of the sample arm, as is the case in the implementation illustrated in **Figure 1.4**. A generic structure of a time domain signal is illustrated in **Figure 1.5a** [28], [29].
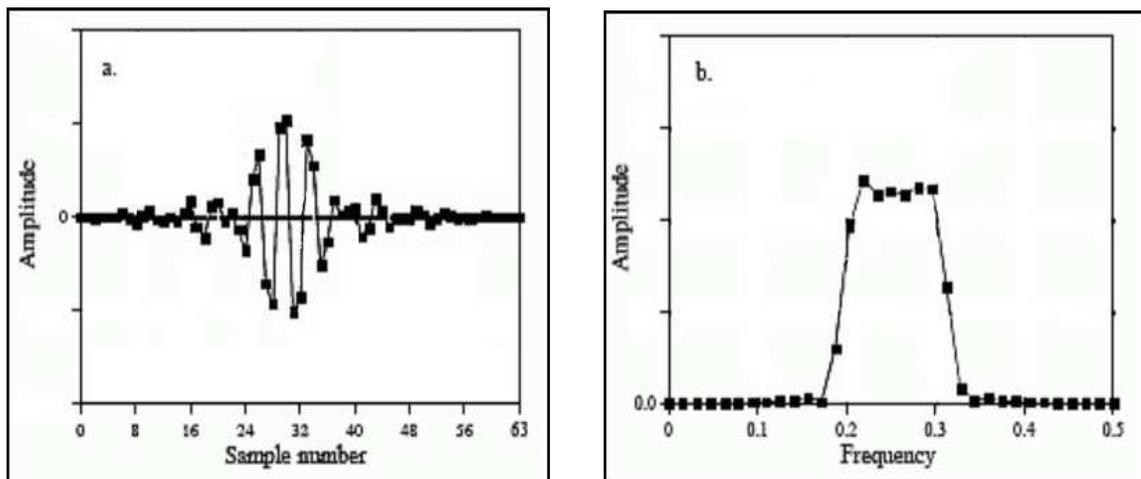
Figure 1.5 Time-Domain & Frequency-Domain Examples

a) A generic time domain signal and b) a generic Fourier domain signal are shown. Both are employed in OCT systems, with Fourier-domain systems being somewhat more common in current implementations.

1.4.2. Fourier Domain OCT. Fourier-domain OCT (FDOCT) is an implementation of OCT in which the interferogram from the system is encoded in the Fourier-domain rather than the time-domain, as is illustrated in **Figure 1.5b**. FDOCT has a number of advantages over current time-domain OCT (TDOCT) techniques. First, the sensitivity of a Fourier-domain system has been shown to be significantly greater than that of a time-domain system. This sensitivity of FDOCT is greater than that of TDOCT because FDOCT collects light from the entire depth of focus of the sample arm while TDOCT only collects light from a single focal length [28]. This collection method also leads to a second advantage of FDOCT over TDOCT; because FDOCT collects information from the entire depth of focus, it is able to render three-dimensional images at a significantly greater speed than TDOCT, which must collect and combine single cross-sectional layers [29].

However, FDOCT does have some disadvantages. Because of the rapid scanning rates seen in FDOCT, high speed CCD's and spectrometers [28] as well as a relatively fast data storage, transmission, and processing equipment are required. FDOCT also has the inherent disadvantage of complex-conjugate-ambiguity resulting from the symmetric properties of the Fourier transform of a real-valued spectral-domain interferometric signal [29]. Complex-conjugate-ambiguity takes the form of a mirror of the sample image overlaid upon the sample image.

1.4.3. Swept Source OCT. Swept-source OCT (SSOCT) is an implementation of Fourier-domain OCT (FDOCT) that employs a Fourier-domain transformation of a interferogram from a high-speed frequency swept laser signal. The swept-source laser produces a series of narrowband light emissions that are rapidly shifted in a sinusoidal manner around a central wavelength. This rapidly swept signal is then used to illuminate both the reference arm and sample arm of the OCT system. The backreflected light from the sample is combined with the reflected reference light to form an interferogram. The interferogram is then transformed into the Fourier domain, from which the three-dimensional and cross-sectional images may be produced [29].

1.4.4. Common Path OCT. A common path interferometer is one in which the sample and reference arms share the same path for all but a small fraction of their lengths. This design helps to significantly reduce any environmental effects, such as

temperature or vibrations, that may affect an interferometer that possesses separate paths for the sample and reference arms. Because the sample and reference arms share the same path and are essentially the same length, the lead-in fiber length for a common path probe can be adjusted as needed [30], [31].

1.5. CURRENT OCT APPLICTIONS

1.5.1. Ophthalmic Imaging. Optical coherence tomography is presently employed for imaging of the human eye. Since OCT is able to to image non-invasively with submicron resolution, imaging of the retina and optical vasculature is possible, aiding in detection of ophthalmic diseases, such as detached retina, and surgical intervention to treat these conditions [20], [32].

1.5.2. Dermatology. The non-invasive, subsurface imaging properties of OCT make it well suited for imaging and assessment of dermatological conditions, such as melanoma. For example, atypical nevus (i.e. dyspastic nevi), a specific type of melanoma, requires extensive examination in order to diagnose the condition. In this case, the subsurface morphological imaging enabled by OCT can expedite the detection of the melanoma with a very high degree of accuracy [33], [34].

1.5.3. Endoscopic Imaging. Barrett's Esophagus is an adaptive endothelial condition in which the esophageal tissue is gradually replaced with stomach tissue. Normally, macroscopic and microscopic tissue imaging as well as a tissue biopsy is needed to properly diagnose Barrett's Esophagus, however endoscopic optical coherence tomography (EOCT) has been shown useful in detecting the condition due to the ability of an EOCT system to produce morphological images with micrometer resolution [35]. While the human trachea, intestines, lungs, and eyes have also been imaged with OCT technology [20], [32], [36], large portions of the human body cannot be imaged with subsurface probes or pulmonary/gastrointestinal endoscopes. As such, the development of a relatively robust intraarterial or intravenous endoscope is desirable for further improvement in the field of OCT. The increased depth of focus in advancing endoscopic probes will allow for the imaging of a larger portion of body tissue.

2. APPLICATION AREAS

2.1. COMMON PATH BEAM-SPLITTING INTERFEROMETER

In OCT systems, a beam splitter is used to split an incident beam into two separate reference and sample arms which are then combined to generate an optical interference signal. The resulting signal can then be computationally analyzed to produce depth profiles (A-Scans), cross-sectional images (B-Scans), and three dimensional images [1].

Because of the inherent interferometric properties of OCT, the interferometer is an important component in an OCT system, regardless of which type of interferometer is employed [37]. In traditional OCT systems, the sample and reference arms exit the beam splitter to form two physically separate arms, which can produce a number of disadvantages, including susceptibility to environmental noise differences between the two arms of the system [38]. Another possible issue when employing separate sample and reference arms is the issue of polarization fading caused by polarization differences arising between the two arms as they propagate separately in space [31]. In addition, endoscopic interferometric probe designs also need to take into consideration the current medical instrumentation that will be used alongside the probe while maintaining a flexible and robust structure.

In order to help decrease the issues in endoscopic OCT probe design, Vakhtin et al [30] proposed a common path interferometer for using in OCT imaging. When employing a common path probe, the specific OCT implementation is then known as common path OCT (CPOCT); in CPOCT the sample and reference arms share the same beam path rather than having separate physical paths in space. This not only helps to reduce the issues of polarization and dispersion mismatch between the two arms of the system, it also helps to reduce the system complexity [30], [39]. Since the initial demonstration of CPOCT by Vakhtin et al in 2003, a number of endoscopic CPOCT probes have been developed, including conical tip fiber probes [40] and side viewing bare fiber probes [31].

In CPOCT probes, a partially reflective surface near the distal endface of the probe functions as the reference plane for the system. Most of the CPOCT probes that have been developed generally require an in-axis reference plane that is positioned at a set distance in front of the sample, which means that the phase matching point (the point at which the optical path difference between the two arms is zero) is positioned at a distance of approximately 2~3mm from the sample. Thus, the interference conditions and fringe visibility within the sample could be considered to be somewhat limited. And, while the CPOCT systems have been shown to possess decreased susceptibility to environmental factors, the reduction in fringe visibility has led to lower sensitivity, contrast, and imaging depth when compared to the more traditional Michelson Interferometer based systems [31].

2.2. BIOCERAMIC ANALYSIS EMPLOYING OCT

Since the initial development of 45S5 bioactive glass by Hench et al. in 1971 [8], bioactive glasses have been shown to possess a notable ability to bond to various tissues and to supplement the growth of bone cells during repair [8] [9], [10], [11]. As such, bioactive glasses have become a fast growing medical utility for applications such as orthopedic implant coatings, dental implants, bone fillers, drug delivery, and tissue engineering scaffolds, with various formulations being applied in these areas.

The compound responsible for the strong bond between the ceramic material and the surrounding tissue is hydroxyapatite (HA), a crystalline form of calcium phosphate, which forms as a film on the surface of bioactive glasses following implantation or immersion in simulated body fluid (SBF) [8]. Characterization of the structural, mechanical, biological, and aging properties of specific formulations and configurations of these glasses is a pertinent issue. Particularly, the conversion of bioactive glass to HA, which can vary greatly depending on the type of the bioactive glass [13], [14], [41], [42].

A number of techniques are involved in the assessment of the properties, such as porosity and HA conversion, of these bioactive glasses, including X-ray microtomography, histological sectioning, and electron microscopy [15]. While each of these techniques provides worthwhile imaging data, they also possess drawbacks that limit their utility for in situ and in vivo assessment of bioactive glasses [4]. X-ray

microtomography is particularly useful for in situ assessment of samples because it is able to render volumetric images and penetrate soft tissue, allowing for in situ subsurface imaging. However, X-ray microtomography possesses both reduced contrast and resolution when compared to other imaging techniques, which limits its utility for assessing histological properties [4], [15].

Histological sectioning and electron microscopy are both able to provide images with high degrees of both resolution and contrast. Yet, both histological sectioning and electron microscopy require sacrificing test animals for imaging purposes, preventing in situ use in test animals. The sacrificial requirement of these techniques results in an increased number of samples to fully assess material properties and changes that occur over time when compared to in situ techniques [12].

As it is currently employed in many biological applications, OCT is capable of penetrating up to approximately 3~4mm of soft tissue to produce cross-sectional and volumetric morphological images with micrometer resolution, without the additional requirement of sacrificing test animals [12]. It is able to produce tomographic images with significantly higher resolution than other modern imaging modalities, including X-ray, ultrasound, MRI, and PET [15].

Unlike histological sectioning and electron microscopy, the penetrative properties of OCT allow for in vivo imaging of samples with little preparation [12], [15]. This in vivo aspect reduces the number of samples required to obtain a set of images depicting the changes which a ceramic scaffold undergoes over time [12]. When assessing the change of a sample over a period of time, OCT also possesses the benefit of real-time imaging, allowing for imaging of rapidly occurring changes within samples. OCT also possesses very high resolution enabling it to produce images with axial resolutions below 10μm, allowing for assessment of histological properties within samples [12]. The high resolution will also allow for the assessment of porosity, defects, and other structural properties of samples. In addition to high resolution, OCT also possesses relatively high contrast when compared to X-ray microtomography [12], [15].

3. RESEARCH

3.1. COMMON PATH BEAM-SPLITTING INTERFEROMETER

3.1.1. Materials and Methods. The following sections detail the procedures employed in the design, fabrication, and testing of the interferometric probe.

3.1.1.1. Design and Fabrication Process. A concentrically symmetric, hollow core, common path interferometric probe was designed and constructed to be used as an OCT probe in an FDOCT for endoscopic applications. **Figure 3.1** shows the schematic diagram of experiment setup. Light from a broadband laser source (BWC-ASE, 1520nm-1620nm) was coupled into a single mode fiber (SMF) and routed to the OCT probe through a fiber circulator. Inside the probe, the SMF was connected to a graded index (GRIN) lens which expanded and collimated the output light.
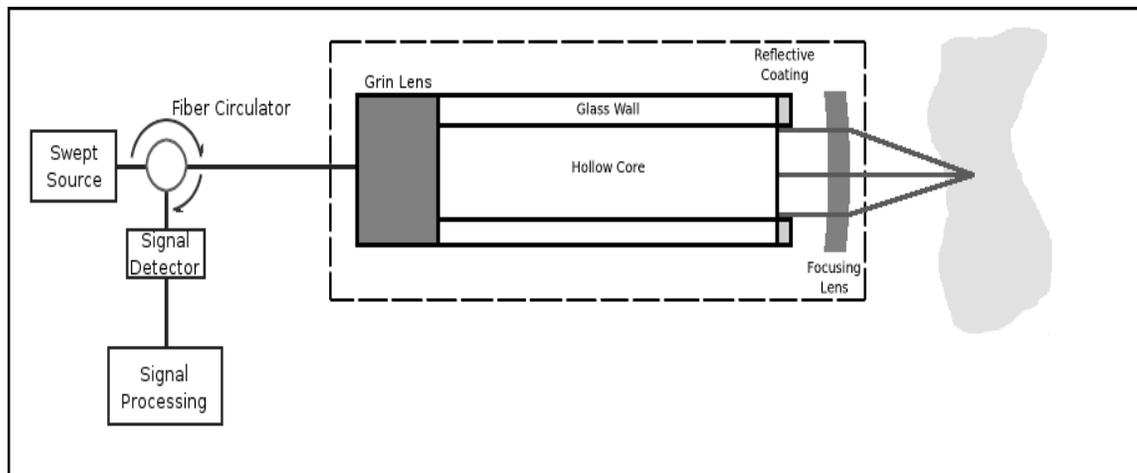
Figure 3.1 CPOCT Hollow Core Probe

Light from a broadband laser source (BWC-ASE, 1520nm-1620nm) was coupled into a single mode fiber (SMF) and routed to the OCT probe through a fiber circulator; inside the probe, the SMF was connected to a GRIN lens which expanded and collimated the output light; the light from the GRIN lens was then coupled into a glass capillary tube, the inner diameter of which was smaller than the FWHM of the GRIN lens.

The light from the GRIN lens was then coupled into a glass capillary tube, the inner diameter of which was smaller than the full width at half max (FWHM) of the GRIN lens.

Because of the relative inner and outer diameters of the glass tube as compared to the diameter of the FWHM of the GRIN lens, part of the incident light enters the glass wall of the tube while the rest travels inside the hollow core of the tube. The light propagating in the tube wall is then reflected from the distal endface of the tube which is coated with a highly reflective gold film. The reflected light then travels backwards within the tube wall and is refocused by GRIN lens into the SMF to serve as a reference. At the same time, the light traveling inside the hollow core of the tube passes through a focusing lens into a tissue sample. The backscattered light from the tissue is collected by the focusing lens and travels backwards to meet the reference beam in the SMF, generating an interference signal. The backward-propagating interference signal is rerouted through the fiber circulator to the detector and is demodulated to obtain the A-scan. A high-resolution motorized translation stage provides the lateral scanning for the B-scan operation through GPIB control. Two scripts were written with Matlab to **a)** operate and collect data from this experimental CPOCT system and **b)** reconstruct a preliminary tissue image from the gathered data.

Because the distal endface of the hollow tube is finely polished and sputter coated with gold film to produce a highly reflective surface, the resulting interferometer possesses multiple, advantageous properties. First, the tube separates light into a sample arm and a reference arm which share the same optical axis (i.e. it is a common path probe); second, the difference in refractive index of propagation media of the two beams combined with a known tube length proerial and length of the tube; third, because the distal tube endface is coated with a highly reflective material, it acts as an in-probe reference plane.

The beam splitting ratio of the interferometer is determined by two major factors; the inner diameter of the hollow core tube, and the reflectivity of the coating on the tube endface. To obtain optimized interference fringes and account for the low amount of light backscattered from biological tissue, the beam splitting ratio should be established so that a larger portion of the light is coupled into the sample arm than the reference arm.

3.1.1.2. Probe Characterization.

In this experiment, tubes with different inner diameters were employed. To ensure that the reference arm was actually returning from the distal endface of the tubes rather than the proximal endfaces of the tubes, the reflected power of the tubes was measured after fine polishing (3μm, UltraPol 1000) but before coating. The reflected powers from the coated tubes (~2 mins Au sputter coating) were then compared to the uncoated tubes, the results of which are shown in **Table 3.1**. All three tubes are roughly the same length (~60mm) and were polished and sputtered under the same conditions.

Table 3.1 Uncoated and Coated Tube Maximum Reflection Power

ID(mm)	Pr uncoated (dBm)	Pr coated (dBm)
0.254	-57.13	-26
0.300	-43.98	-28
0.319	-44.65	-30

To measure the power splitting ratio of each tube, the light field profile at a distance from the tube endface was mapped by scanning the output of the tube in both axial directions; as an example, the transmission profile for the light exiting the 0.300mm inner diameter tube is shown in **Figure 3.2a**. The transmission profile of a GRIN lens is also plotted for comparison in **Figure 3.2b**.

As shown in **Figure 3.2**, the light field profile exiting a GRIN lens is a clean Gaussian distribution, and the light filed profile exiting the glass tube is close to a Gaussian shape, although some random ripple structure is present. The power splitting ratio was then calculated by dividing the power propagating within the inner diameter of the tube by the total incident light power and integrating. Considering the absorption within the glass to be negligible, the resulting power splitting ratios are given in **Table 3.2**.
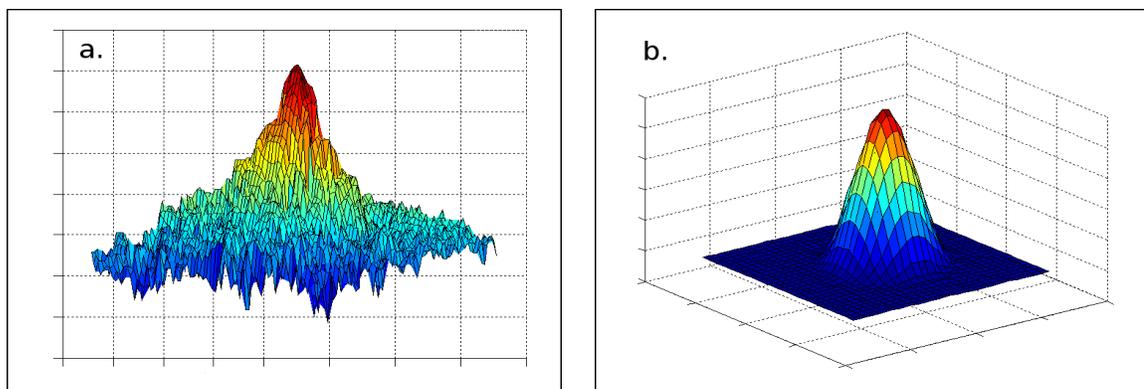
Figure 3.2 Transmission Profiles for Hollow Tube & GRIN Lens

*a) The transmission profile for the light exiting a 0.300mm inner diameter hollow core glass tube and **b**) the transmission profile for a 0.25 pitch GRIN lens both possess generally Gaussian shapes.*

From **Table 3.1**, it can be seen that the gold coating on the tube endface increases the reflected power by approximately 15~20dB. Additionally, **Table 3.2** shows that the power splitting ratios for the three sample tubes are all fairly high, which is ideal for imaging biological systems in which much of the light in the sample arm will be scattered away from the imaging axis and thus cannot be detected.

Table 3.2 Coated Tube Power Splitting Ratios

ID (mm)	0.254	0.300	0.319
PSR	88.041%	93.857%	96.040%

3.1.2. Results. For a preliminary phantom specimen, a stack of three thin glass cover slips were adhered together with a small amount of water and imaged using the probe. Each glass slide was approximately 140µm thick. The OCT system was able to detect the front and rear surfaces of the slides due to the water-glass and glass-water interfaces. The detected interference signal is shown in **Figure 3.3**.
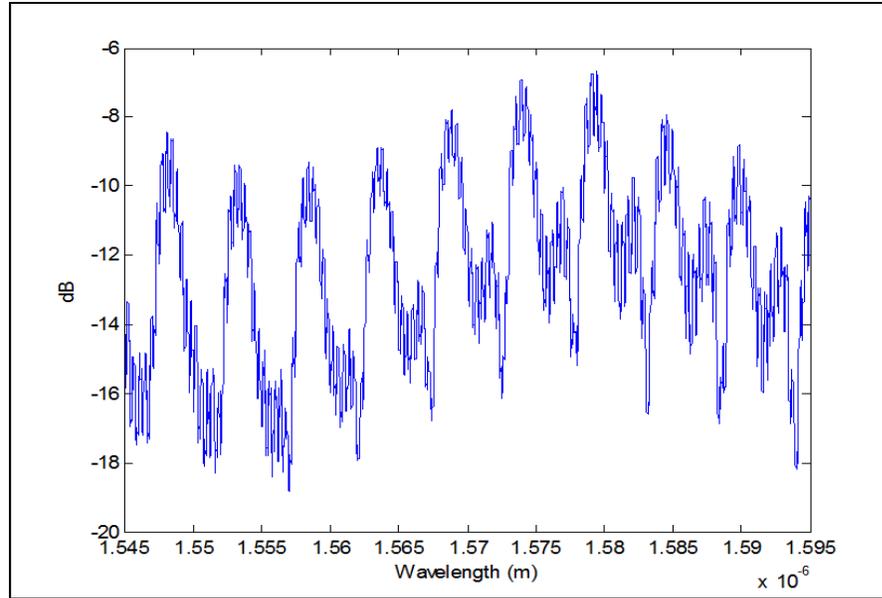
Figure 3.3 OCT Interference Signal

The signal was obtained using a Yokogawa optical spectrum analyzer (OSA); the envelope is the interference between multiple layers of the sample, and the small fringes are the interference between the coated tube endface and the sample.

The Fourier transform of the interference signal isv shown in **Figure 3.4**, and **Figure 3.5** then depicts a cross-section OCT tomogram of the sample. The resulting image size is 31x31 (x-y) pixels giving an area of 155μm x 155μm. The step-size used on the translation stage used for the scanning was 5μm. The four light/dark planes in **Figure 3.5** show the interfaces within the sample.

As is shown in **Figure 3.5**, the four dark lines indicate the interfaces of the glass slides. The average thickness of the glass slides calculated from the image is 150μm, which is very close to the actual thickness of 140μm. Similarly, **Figure 3.6** shows the three dimensional reconstruction of the cover slip sample.
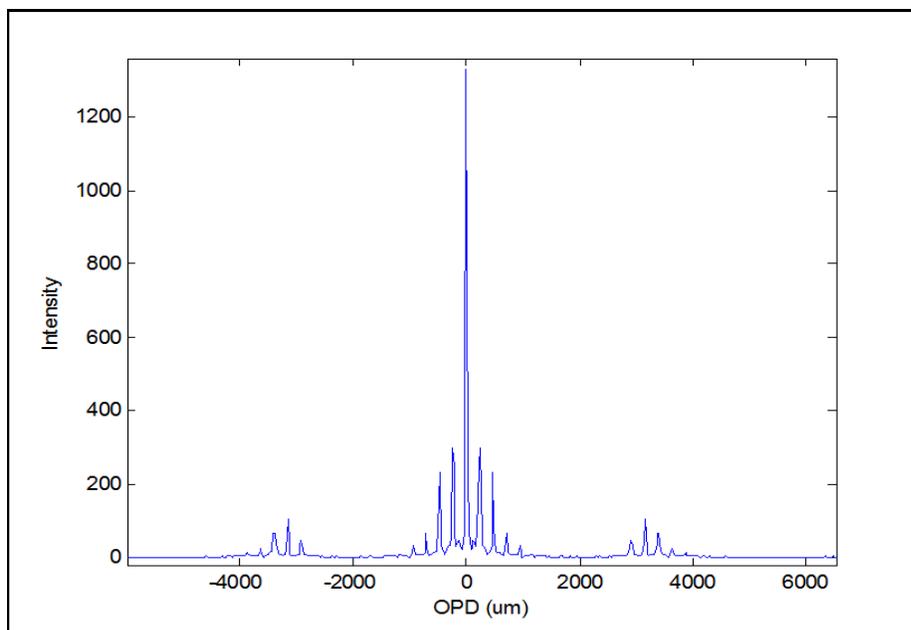
Figure 3.4 Fourier Transform of an OCT Interference Signal

There are several peaks in the middle of the image, which correspond to the interferences between the cover slips, which are undesired for OCT imaging. The peaks at the two sides (near +/- 3000) correspond to the interferences of the tube endface and the cover slips.
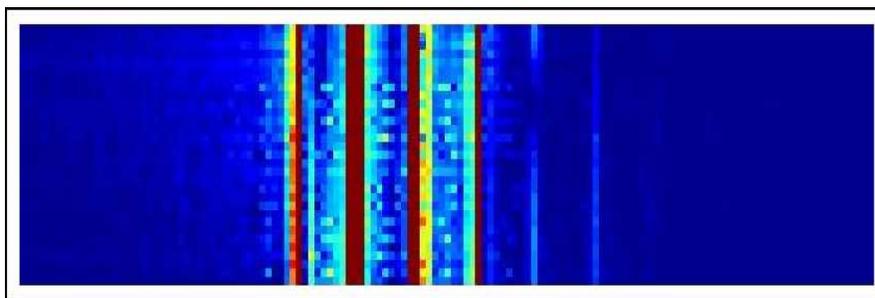
Figure 3.5 Cross Sectional Tomogram

The tomogram is the result of image reconstruction of the interferogram. The dark/light vertical planes indicate the glass-air and air-glass interfaces.
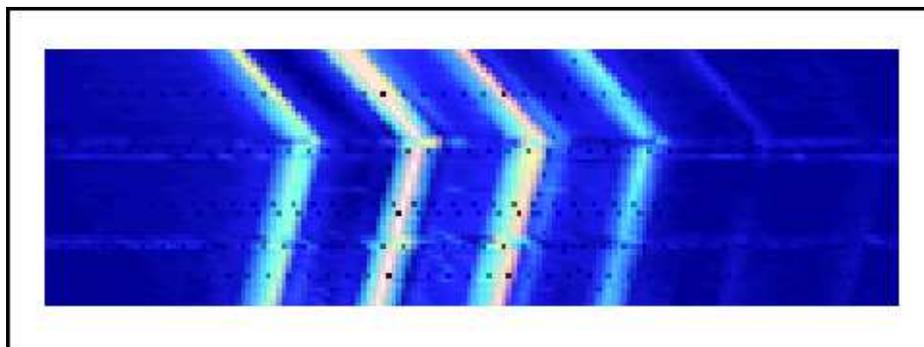
Figure 3.6 Three Dimensional Tomogram
The image was reconstructed from a simple cover slip sample.

3.1.3. Discussion. Thus, a concentrically symmetric, hollow core, beam splitting probe has been developed and demonstrated for CPOCT. The preliminary imaging of glass cover slips shows that clear interfaces are observable within a volumetric imaging configuration. The probe can be readily fabricated via polishing and sputtering techniques at relatively low cost and with high reproducibility.

The eventual aim of this research is to encapsulate the probe in a surgical steel housing for integration with a commercially available OCT system and investigation of possible medical applications. The use of such a CPOCT system may be promising for endoscopic application because of its small size, robust structure, and high resolution. However, it is worth noting that the current design which includes a reflective coating will likely need to be modified to withstand cleaning procedures such as autoclaving.

3.2. BIOCERAMIC ANALYSIS EMPLOYING OCT

3.2.1. Materials and Methods. The following subsections detail the procedures employed in the investigation of the utility of OCT for imaging of ceramic bioscaffolds.

3.2.1.1. Preparation of Bioactive Glass Scaffolds. Borate doped 1393 bioactive glass scaffolds, with two-thirds of the silica content replaced with borate, were prepared by members of the Missouri S&T Department of Ceramic Engineering

using a polymer foam replication technique as previously described by Fu et al. [43]. The resulting microstructure is generally comparable to human trabecular bone.

3.2.1.2. Structural Characterization of the Glass Scaffolds.

Optical coherence tomography (Thor Labs OCS1300SS) was employed to observe the microstructure of the scaffolds before and after immersion in a high phosphate concentration SBF (0.02 M K_2HPO_4, starting pH=7.0 at 37ºC), which was used to accelerate the aging of the scaffolds when compared to standard SBF. The porosity of the scaffolds was then derived from the resulting images using edge detection algorithms.

3.2.1.3. Hydroxyapatite conversion of the Glass Scaffolds. The

in vivo bioactivity of the glass scaffolds after immersion in SBF was assessed by comparing OCT results with SEM images of the scaffolds after set durations of immersion. Initial imaging was performed with dry, unimmersed scaffolds, followed by imaging of scaffolds after a brief immersion in SBF.

3.2.2. Results. OCT and SEM images of the previously described borate doped

1393 bioactive glass scaffolds are shown in **Figure 3.7** with an additional image of dry human trabecular bone.
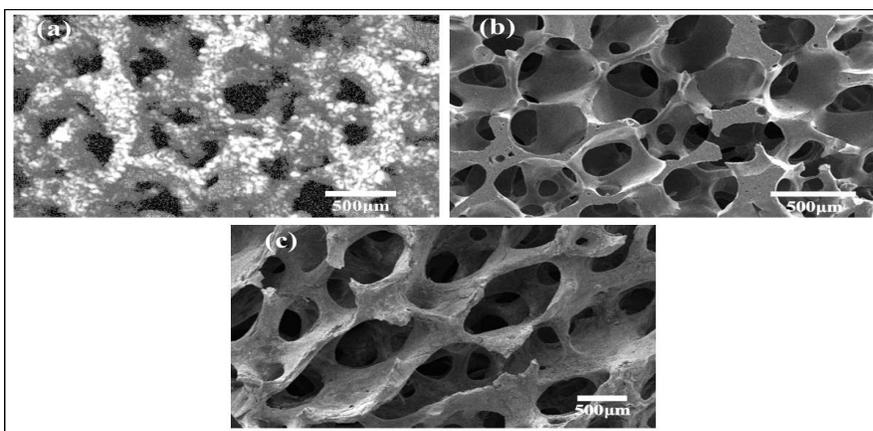
Figure 3.7 OCT and SEM Image comparision

a) An OCT image of a borate doped scaffold, b) an SEM image of a borate doped scaffold produced using the same process, c) and an SEM Image of trabecular bone are shown.

The structure of the ceramic scaffold is very similar to that of the trabecular bone in both the OCT and SEM images. In addition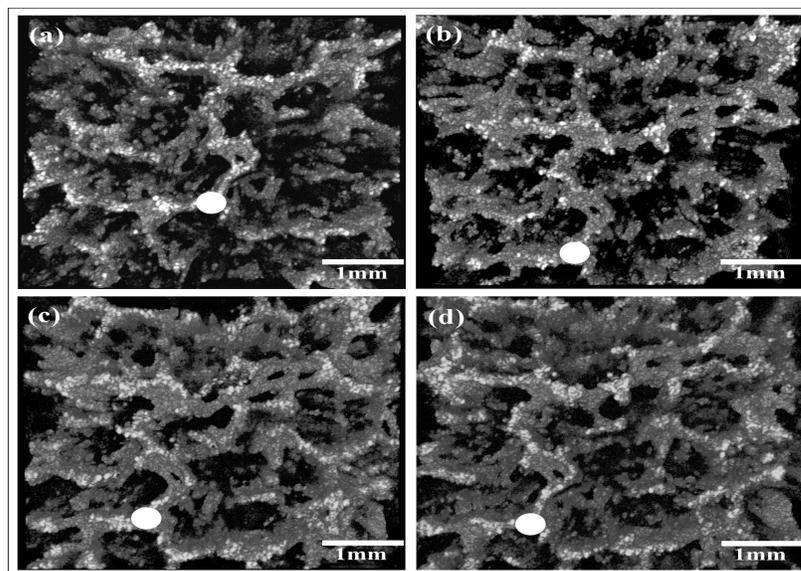, regular OCT imaging was done using a single scaffold in order to demonstrate the non-destructive properties of OCT to measure changes over time; a selection of the resulting images is shown in **Figure 3.8**.

Figure 3.8 Sequential OCT Imaging

OCT images taken after a) 3 days, b) 5 days, c) 7 days, and d) 9 days of aging in high phosphate SBF are shown. The white circle identifies a single common location within each scan of the scaffold.

Using the data collected from the OCT imaging, the porosity of a scaffold was calculated using edge detection and the contrast information in the OCT data files. **Table 3.3** compares the resulting OCT based porosity calculation with the porosity of the same scaffolds calculated using the Archimedes method. It can be seen from **Table 3.3** that the percent difference between the porosity calculated using the OCT data and the porosity calculated using Archimedes Method is less than 1%.

Table 3.3 Comparison of Porosity from OCT Calculation and Archimedes Method

Sample	Archimedes Porosity (%)	OCT Porosity (%)	Percent Difference (%)
1	75.62	75.48	0.19
2	71.45	71.57	0.17
3	75.75	75.25	0.66

Comparative images of OCT and x-ray microtomography scans are shown in **Figure 3.9**. It can be seen from the images that OCT presents a significantly higher degree of resolution, however, x-ray microtomography does have the advantage of deeper penetration with respect to the width of the image. X-ray microtomography also has the additional benefit of robust suites of previously developed image processing tools, which is evident in smoothed and cleaned image that is presented in **Figure 3.9a**.
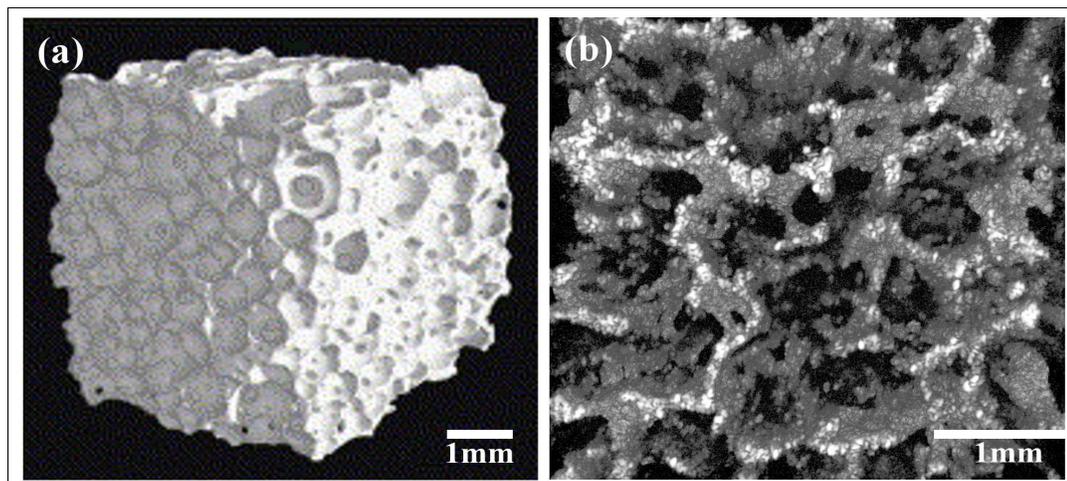
Figure 3.9 Comparison of X-Ray Microtomography and OCT Images

*Shown are **a)** a typical volumetric OCT scan of a scaffold, **b)** a typical volumetric x-ray microtomography scan of a scaffold of the same composition and fabrication procedure.*

3.2.3. Discussion.   The resulting data shows that OCT has the ability to provide useful data for bioactive glass scaffold analysis. The similarity between the OCT and SEM images shown in **Figure 3.7** demonstrates the capability of high resolution imaging of an OCT system that approaches the resolution of an SEM image. In addition, the OCT imaging can be performed in vivo, while SEM imaging requires drying and metal coating before imaging can be performed. Also, the OCT images presented in **Figure 3.7** and **Figure 3.8** are composed of the data taken from the sections located between 1mm and 2.5mm of depth within the volumetric scans of the scaffolds. As such, the images presented demonstrate the subsurface imaging capabilities of OCT for bioactive ceramic scaffold imaging.

The small percent difference between the porosity calculated using OCT and that determined through the use of Archimedes method shown in **Table 3.3** demonstrates that the raw data from OCT imaging can provide additional benefits to simple imaging when employing the computational data for various uses.

Figure 3.9 shows that OCT possesses similar imaging capabilities to that of x-ray microtomography. While the depth at which OCT is able to operate is less than that of x-ray microtomography, OCT is able to image the available depth with significantly higher resolution and contrast.

A swept source OCT imaging system was used to investigate the utility of OCT for hard tissue and ceramic bioscaffold surface imaging. The preliminary test on the imaging of the bioactive glass scaffolds is encouraging and shows that the OCT modality can produce in vivo imaging results with resolution comparable to that of SEM imaging. In addition, it is able to provide volumetric scanning capabilities comparable to x-ray microtomography, from which porosity can be calculated computationally. The resolution for the probe used in this work was measured to be 6μm axially and 12μm laterally.

4. CONCLUSION

4.1. SUMMARY

A hollow core, concentrically symmetric, beam-splitting Michelson Interferometer for common path optical coherence tomography has been designed and constructed. The imaging probe was used to image some preliminary tissue phantoms; depth profiles, cross sectional images, and three dimensional volumetric maps were reconstructed from the interferometric data. It has been demonstrated that the device does function as an imaging probe. Additionally, papers has been prepared for submission to Applied Optics and the Journal of Biomedical Optics.

A swept source OCT imaging system was used to investigate the utility of OCT for ceramic bioscaffold imaging. The preliminary imaging of the bioactive glass scaffolds is encouraging and shows that the OCT modality can produce in vivo imaging results with resolution greater than that of x-ray microtomography. In addition, it is able to provide volumetric scanning capabilities comparable to x-ray microtomography. Since the volumetric data is stored as intensity data rather than image data, the raw OCT data can be used for additional computational assessment, such porosity calculation and defect detection. The small percentage difference between the OCT porosity calculations and the reference Archimedes Method measurements demonstrates the additional benefits that can be realized though data manipulation and processing.

While OCT imaging is usually limited to surface and soft tissue imaging due to tissue penetration issues, the imaging performed in this research does show a degree of utility for imaging silica structures. Also, the resolution of the probe used in the bioceramic imaging was measured to be 8μm radially and 12μm depth-wise, demonstrating the high resolution capabilities of OCT imaging.

4.2. FUTURE WORK

One aim of this research is to encapsulate the hollow core probe in a surgical steel housing to ease alignment and prepare the probe for integration with a commercially available OCT system, enabling investigation of possible medical applications. The use

of such a CPOCT system may be promising for endoscopic application because of its small size, robust structure, and high resolution.

The eventual aim of the bioscaffold research is to investigate the use of OCT as a in vivo tool for imaging of ceramic bioscaffolds following cultured tissue growth and implantation in animal models. Some preliminary imaging of test animal implantations has already been performed, as well as some preliminary imaging of healthy human tissue.

APPENDIX A

ADDITIONAL IMAGES
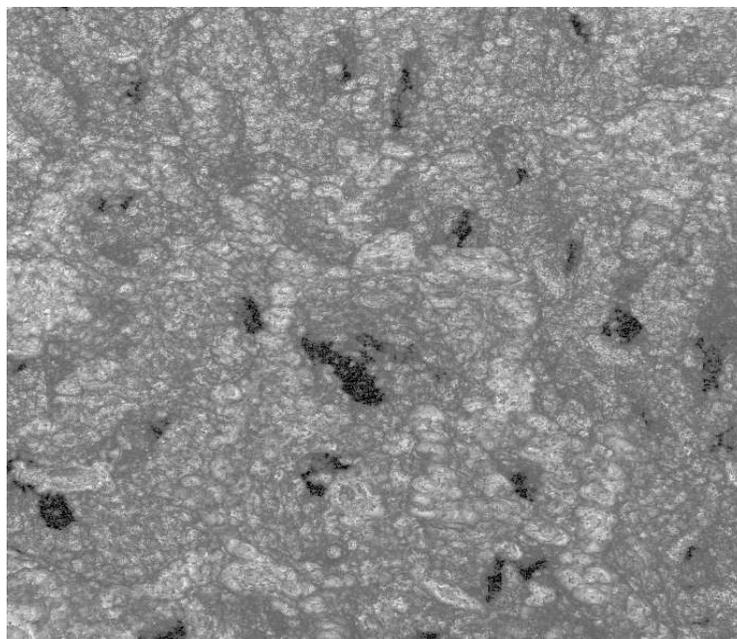
Figure A.1 Volumetric Image of a Trabecular Scaffold
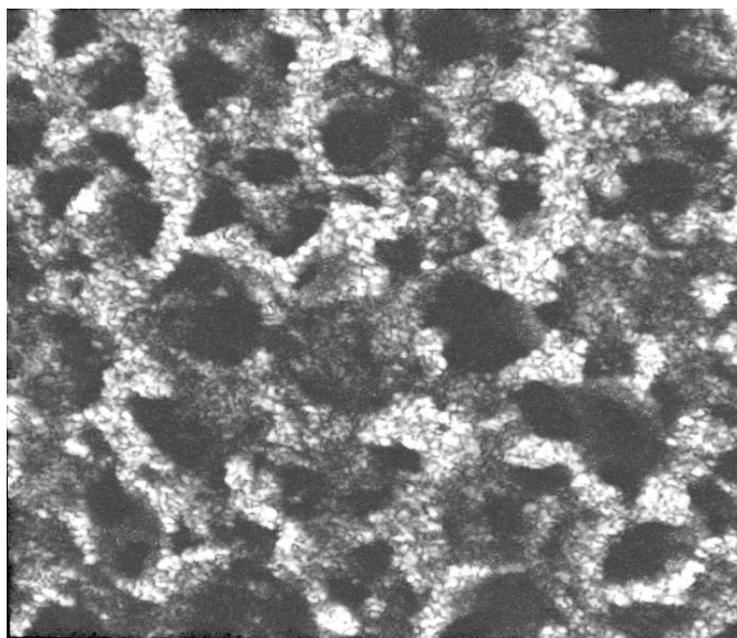
Figure A.2 Volumetric Section of a Trabecular Image (~200nm thick)
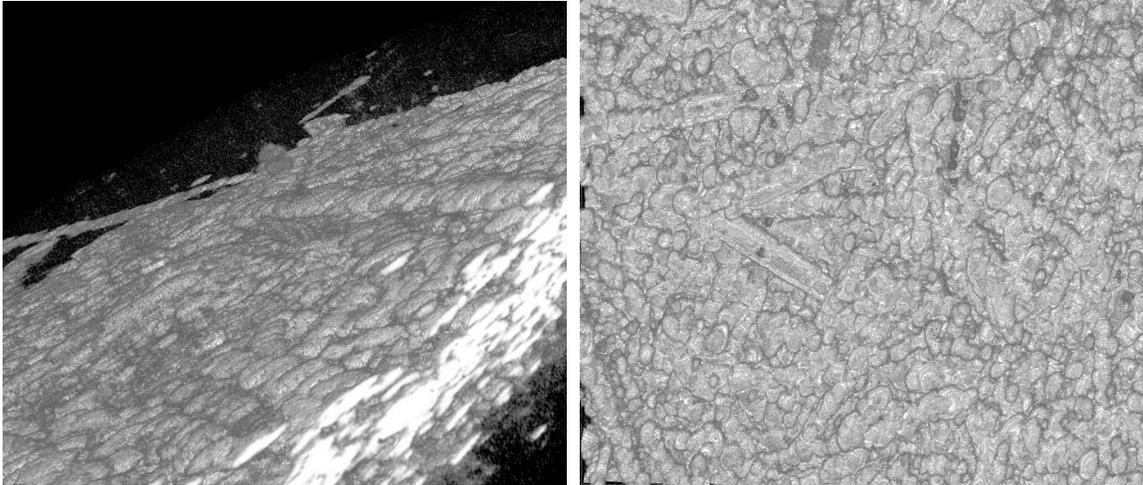
Figure A.3 OCT Image of Bioglass "Cotton Ball"

Loose random bioglass fibers were formed into a cotton-ball like structure. A small amount of the fiber ball was flattened then imaging.
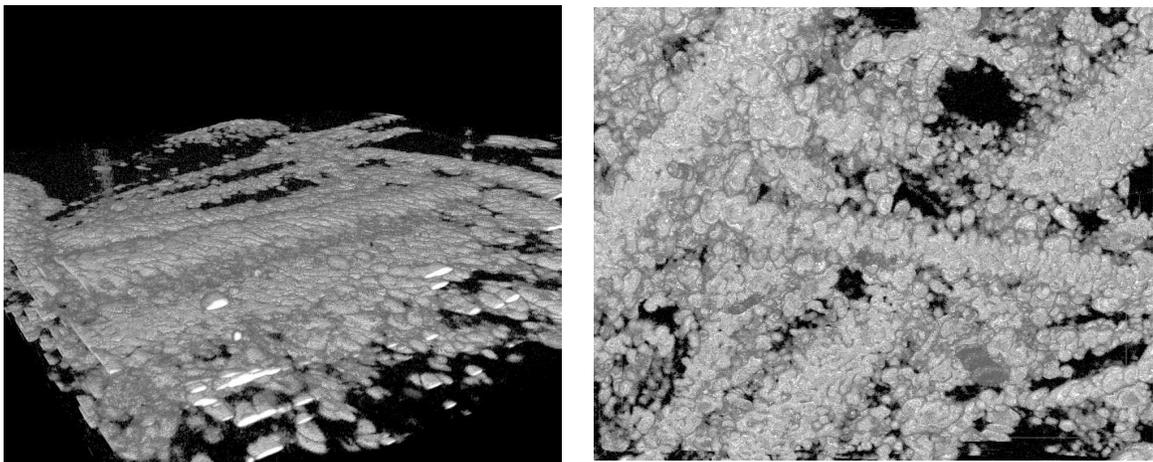
Figure A.4 Section of an OCT Image of Bioglass "Cotton Ball"

A scaffold composed of random bioglass fibers was scanned. A thin section of the scaffold's volumetric map was selected before outputing the images.
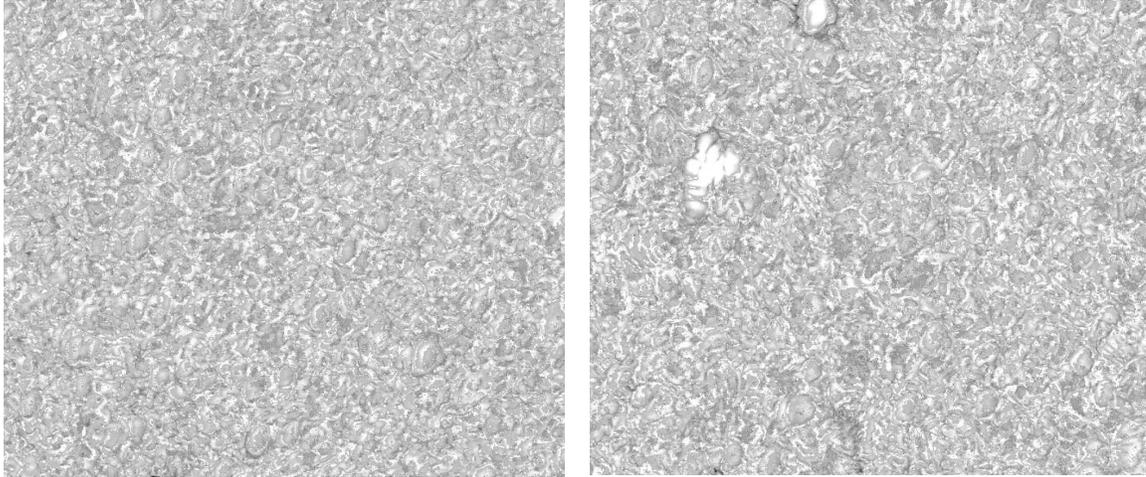
Figure A.5 OCT images of a thick (~15 mil) PCL/Bioglass Composite

Images of a composite sheet composed of polycaprolactone (PCL) polymer and bioglass beads are shown. The left image is the rougher surfaced upper side and the right image is the smoother surfaced lower side.
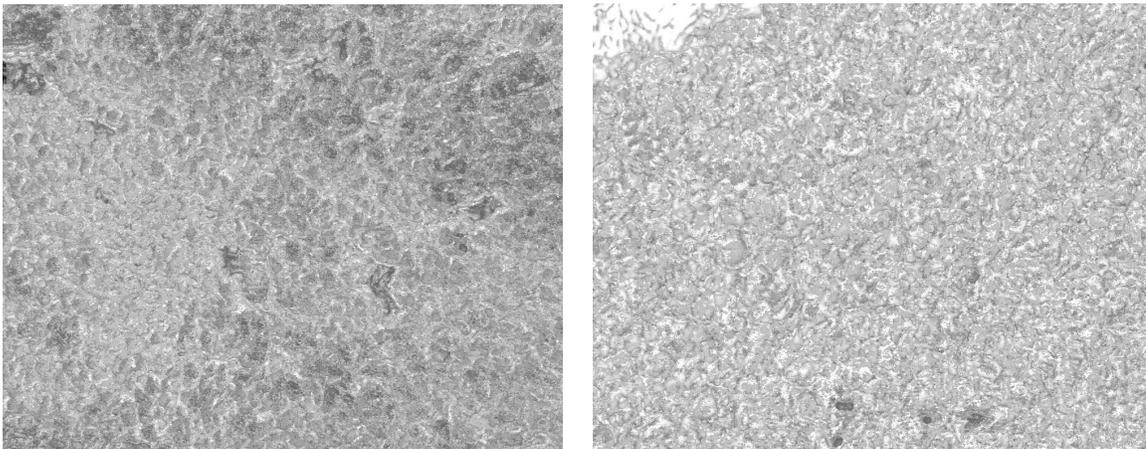
Figure A.6 OCT imaging of a medium (~10 mil) PCL/Bioglass Composite

Images of a composite sheet composed of polycaprolactone (PCL) polymer and bioglass beads are shown. The left image is the rougher surfaced upper side and the right image is the smoother surfaced lower side.
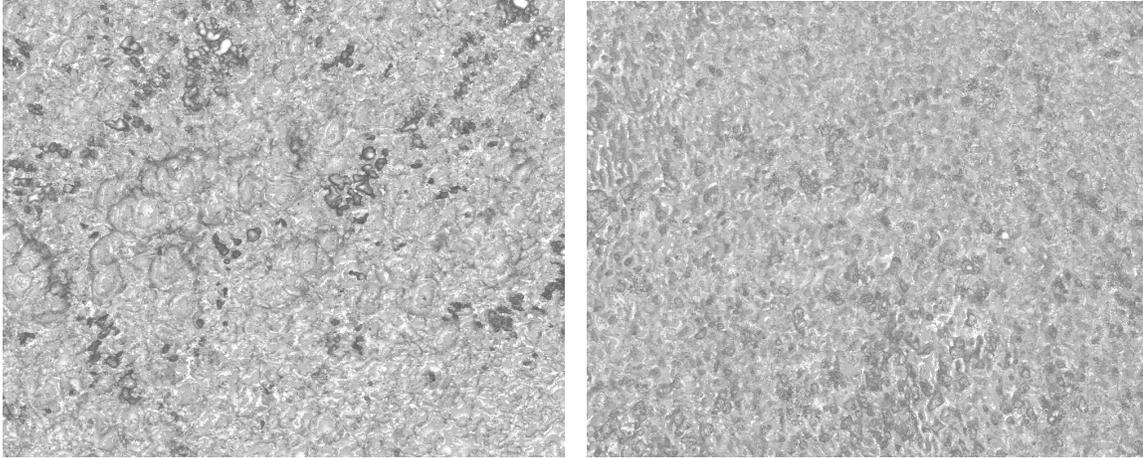
Figure A.7 OCT imaging of a thin (~5 mil) PCL/Bioglass Composite

Images of a composite sheet composed of polycaprolactone (PCL) polymer and bioglass beads are shown. The left image is the rougher surfaced upper side and the right image is the smoother surfaced lower side.

APPENDIX B

MATLAB SCRIPTS

B.1 OCTRead.m. This function reads the the OCT signal.

```
%% Opening Cleanup
% Read interference data from Concentric OCT Probe
clc
clear all
close all
format compact

%% Set Data Points to be Read
warning on verbose
warning off MATLAB:unknownObjectNowStruct
warning off MATLAB:UndefinedFunction
warning off MATLAB:unknownElementsNowStruc
load('yn_5_4_2011.mat')
warning on MATLAB:unknownObjectNowStruct
warning on MATLAB:UndefinedFunction
warning on MATLAB:unknownElementsNowStruc

%% Begin Loop to Run Through Entire Array
[p,q,r]=size(Mesh_A);

InterferenceMatrix=zeros(p,r,10146);

m=1;
for jj=1:p
    n=jj;
    for kk=1:r
        o=kk;

%% Gather Data From a Single Sample Point
OCTInterference(1,:) = data(n,m,o,:);
OCTInterference = OCTInterference - ref';

%% Allocate the Coordinates of a Single Sample Point
Acoord = Mesh_A(n,m,o);
Bcoord = Mesh_B(n,m,o);
Ccoord = Mesh_C(n,m,o);

%% Stage Stepsize in Meters
OCTstepsize=1e-6;

%% Convert the Wavelength Vector to a Wavenumber Vector
OCTwavenumber=wl2freq(X.*1e9);
OCTminwave=min(OCTwavenumber);
OCTmaxwave=max(OCTwavenumber);
OCTwavearray=OCTminwave:OCTstepsize:OCTmaxwave;
OCTwavearraylength=length(OCTwavearray);

OCTFFTxaxis=1/(OCTmaxwave-OCTminwave)*[floor(-
OCTwavearraylength/2):floor(OCTwavearraylength/2-1)]/2;

%% Convert From dB scale to Linear Scale
OCTamplitude=f2b(10.^(OCTInterference./10));
```

```
OCTamplitude1=interp1(OCTwavenumber,OCTamplitude,OCTwavearr
ay);
OCTpathdiff=1/(OCTmaxwave-OCTminwave);
OCTpower=fft(OCTamplitude1);
OCTabspower=abs(OCTpower);

%% Apply ChebyShev Filter to Interference Signal
[ChebyB,ChebyA]=cheby1(2,3,0.008,'high');
OCTfiltered=filtfilt(ChebyB,ChebyA,OCTamplitude1);
OCTfiltFFT=abs(fftshift(fft(OCTfiltered)));

%% Compile Matrix of All Filtered Signals
InterferenceMatrix(n,o,:)=OCTfiltFFT(1,
[floor(length(OCTfiltFFT))/2:floor(length(OCTfiltFFT))]);

end
end

%% Plot the Interference Signal with a dB scale
figure(1)
plot(X,OCTInterference)
ylabel('dB')

%% Plot the FFT of the Interference Signal With a Linear
Scale
figure(2)
plot(OCTFFTxaxis,fftshift(OCTabspower));

%% Plot the Filtered FFT
figure(3)
plot(OCTFFTxaxis,fftshift(abs(fft(OCTfiltered))));

%% Plot Using IMTOOL
Interference2D=squeeze(InterferenceMatrix(1,:,:));
Interference2D=Interference2D*255/
(max(max(Interference2D))-min(min(Interference2D)));

imtool(Interference2D,jet)
```

B.2 f2b.m. This function reverses the order of an array.

```
% backward order
function back=f2b(forth)
kk=length(forth);
for m=1:kk
    back(m)=forth(kk+1-m);
end
back=back';
```

B.3 wl2freq.m. This function converts from wavelength to frequency.

```
% wl to freq
function wavenumber=wl2freq(wl)
len=length(wl);
for m=1:len
    wavenumber(m)=1/wl(len+1-m)*10^3;
end
wavenumber=wavenumber';
```

B.4 wl2wn.m. This function converts from wavelength to wavenumber.

```
% Wavelength to Wavenumber Conversion
%
% Converts a 1D wavelength array to a 1D wavenumber array

function wl2wnout=wl2wn(wl2wnin)

[jj,kk]=size(wl2wnin);

wl2wnout=zeros(size(wl2wnin));
if kk==1;
    for m=1:jj
        wl2wnout(m)=1/wl2wnin(jj+1-m)*10^3;
    end
else
    disp('ERROR');
    disp('The input array for wl2wn is not 1D');
    disp('The function wl2wn is only appropriate for 1D
arrays');
end

wl2wnout=wl2wnout';
```

B.5 OCTFFT.m. This function performs the FFT of an interferogram.

```matlab
%OCT FFT

%% Opening Cleanup
clc
clear all
close all
format long e

%% Load the Data
for i=1:20
    num=i;
    str=num2str(num);
    mark=strcat('L:\Experiment
data\OCT\01072011\',str,'.csv');
    inputdata=load(mark);

%% Establish Parameters & Define Basic Input Arrays
stepsize=1e-6;

%Separate out the amplitude vector
amplitudein=inputdata(:,2);

%Separate out the wavelength vector
wavelengthin=inputdata(:,1);

%% Convert Array Types
%Convert wavelength vector to a wavenumber vector
wavenumber=wl2freq(wavelengthin);
minwave=min(wavenumber);
maxwave=max(wavenumber);
wavearray=minwave:stepsize:maxwave;
wavearraylength=length(wavearray);

%Convert aplitude vector to a reflectance vector
basereflect=10.^(amplitudein./10);
basereflect2=f2b(basereflect);
reflect=interp1(wavenumber,basereflect2,wavearray);

reflectpower=fft(reflect);
abspower=abs(reflectpower);

pathdiff=1/(maxwave-minwave)*(0:wavearraylength-1);

    state(i,:)=abspower(2:50)
end
state

%find the maximum and minimum intensity in the matrix
max1=max(state');
max2=max(max1);
min1=min(state');
min2=min(min1);
```

```
%normalize
% statenorm=state*255/(max2-min2);
statenorm=state./(max2-min2);

%create image
figure
% imshow(statenorm,[0,255]);
imshow(statenorm,[0,1]);
xlabel('Axial depth profile(um)');
ylabel('Lateral scan distance(um)');
set(gca,'XTick',0:13.6:20*13.6);
set(gca,'XTickLabel',
{'0','13.6*100','13.6*200','13.6*300'});
```

B.6 linearization.m. This function linearizes an input.

```
%% Opening Cleanup
clear all
clc

%% Run through
counter=1; %number of Temps

for Temp=100; %sweep scipt
    str=num2str(Temp);
    mark=strcat(str,'.csv');
    if exist(mark)==2
            input=load(mark);
    end
end

inputdata=input(:,2);
ref=load('new ref.csv');
refdata=ref(:,2);
inputdata=inputdata-refdata;
data=10.^(inputdata./10);
wl=input(:,1);
wn=wl2freq(wl);
bdata=f2b(data);

%% Get V
max=max(bdata);
min=min(bdata);
V=(max-min)/(max+min);

%% Plot
figure
plot(wn,bdata)
```

B.7 OCTdist.m. This function determines OCT FFT interface distances.

```
% OCT FFT interface detection
%
% [peakdiffumpos,peaks,peakpoints]=OCTdist(inputdata);
%
% Use this format for input of data
% The 25 is for getting rid of header junk
% inputdata=csvread('2.CSV',25);

function [peakdiffumpos,peaks,peakpoints]=OCTdist(inputdata)

%% Establish Parameters & Define Basic Input Arrays
stepsize=1e-6;

%Separate out the amplitude vector
amplitudein=inputdata(:,2);

%Separate out the wavelength vector
wavelengthin=inputdata(:,1);

%% Convert Array Types
%Convert wavelength vector to a wavenumber vector
wavenumber=wl2freq(wavelengthin);
minwave=min(wavenumber);
maxwave=max(wavenumber);
wavearray=minwave:stepsize:maxwave;
wavearraylength=length(wavearray);

%Convert aplitude vector to a reflectance vector
basereflect=10.^(amplitudein./10);
basereflect2=f2b(basereflect);
reflect=interp1(wavenumber,basereflect2,wavearray);

reflectpower=fft(reflect);
abspower=abs(reflectpower);

pathdiff=1/(maxwave-minwave)*(0:wavearraylength-1);

powershift=fftshift(abspower);
% peaks=zeros(size(powershift));

%% 2 point nearest neighbor peak identification
l=1;
for k=2:(length(powershift)-1)
    if powershift(k)>200
        if powershift(k)>=powershift(k-1)
            if powershift(k)>=powershift(k+1)
                    peaks(l)=powershift(k);
                    peakpoints(l)=pathdiff(k);
                    l=l+1;
            end
        end
    end
```

```
        end

        %% position of peak identification
        m=0;
        for q=1:length(peaks)
            if peaks(q)>m
                maxpos=q;
                m=peaks(q);
            end
        end

        %% conversion of peak postions to um
        peakdiff=abs(peakpoints-peakpoints(maxpos));
        ri=1.45;
        peakdiffum=peakdiff/(ri*2);

        q=1;
        for p=1:length(peakdiffum)
            if peakdiffum(p)>=0
                peakdiffumpos(q)=peakdiffum(p);
                q=q+1;
            end
        end
```

BIBLIOGRAPHY

[1] Welzel J, "Optical Coherence Tomography in Dermatology - A Review," *Skin Research and Technology*, 7.1 (2001) 1-9

[2] Zysk AM, Nguyen FT, Oldenburg AL, Marks DL, Boppart SA, "Optical Coherence Tomography - A Review of Clinical Development from Bench to Bedside," *Journal of Biomedical Optics*, 12.5 (2007) 051403

[3] Huang D, Swanson EA, Lin CP, Schuman JS, Stinson WG, Chang W, Hee MR, Flotte T, Gregory K, Puliafito CA, Fujimoto JG, "Optical Coherence Tomography," *Science*, 254.5035 (1991) 1178-1181

[4] Zeitler JA, Gladden LF, "In-Vitro Tomography and Non-Destructive Imaging at Depth of Pharmaceutical Solid Dosage Formss," *European Journal of Pharmaceutics and Biopharmaceutics*, 71.1 (2008) 2-22

[5] Thomas D, Duguid G, "Optical Coherence Tomography - A Review of the Principles and Contemporary Uses in Retinal Investigation," *Eye*, 18.6 (2004) 561-570

[6] Wojtkowski M, Bajraszewski T, Targowski P, Kowalczyk A, "Real-Time In-Vivo Imaging by High-Speed Spectral Optical Coherence Tomography," *Optics Letters*, 28.19 (2003) 1745-1747

[7] Pierce MC, Strasswimmer J, Park BH, Cense B, de Boer JF, "Advances in Optical Coherence Tomography Imaging for Dermatology," *Journal of Investigative Dermatology*, 123.3 (2004) 458-463

[8] Hench LL, Splinter RJ, Allen WC, Greenlee TK, "Bonding Mechanisms at the Interface of Ceramic Prosthetic Materials," *Journal of Biomedical Materials Research*, 5.6 (1971) 117-141

[9] Hench LL, "Bioactive Materials - The Potential for Tissue Regeneration," *Journal of Biomedical Materials Research*, 41.4 (1998) 511-518

[10] Wheeler DL, Stokes KE, Park HM, Hollinger JO, "Evaluation of Particulate Bioglass in a Rabbit Radius Ostectomy Model," *Journal of Biomaterials Research*, 35.2 (1997) 249-254

[11] Wheeler DL, Stokes KE, Hoellrich RG, Chamberland DL, McLoughlin SW, "Effect of Bioactive Glass Particle Size on Osseous Regeneration of Cancellous Defects," *Journal of Biomedical Materials Research*, 41.4 (1998) 527-533

[12] Walther J, Gaertner M, Cimalla P, Burkhardt A, Kirsten L, Meissner S, Koch E, "Optical Coherence Tomography in Biomedical Research," *Analytical and Bioanalytical Chemistry*, 400.9 (2011) 2721-2743

[13] Day DE, White JE, Brown RF, McMenamin KD, "Transformation of Borate Glasses into Biologically Useful Materials," *Glass Technology*, 44.2 (2003) 75-81

[14] Han X, Day DE, "Reaction of Sodium Calcium Borate Glasses to form Hydroxyapatite," *Journal of Materials Science: Materials in Medicine*, 18.9 (2007) 1837-1847

[15] Jones JR, Lee PD, "Bioactive Glass Scaffolds with Hierarchical Struture and Their 3D Characterization," *Key Engineering Materials*, 441.123 (2010) 123-137

[16] Singer AJ, Clark RAF, "Cutaneous Wound Healing," *New England Journal of Medicine*, 341.10 (1999) 738-746

[17] Devgan L, Bhat S, Aylward S, Spence RJ, "Modalities for the Assessment of Burn Wound Depth," *Journal of Burns and Wounds*, 5.2 (2006) 7-15

[18] Buckman AB, "Guided Wave Photonics," Oxford University Press, Chapter 1-3, 9, (1995)

[19] Verdeyen JT, "Laser Electronics (3rd Edition)," Prentice Hall, Chapter 1, (1995)

[20] Thomas D, Duguid G, "Optical Coherence Tomography - A Review of the Principles and Contemporary Uses in Retinal Investigation," *Eye*, 18.6 (2004) 561-570

[21] Schmitt JM, "Optical Coherence Tomography (OCT) - A Review," *IEEE Journal of Selected Topics in Quantum Electronics*, 5.4 (1999) 1205-1215

[22] Verdeyen JT, "Laser Electronics (3rd Edition)," Prentice Hall, Chapter 9, (1995)

[23] Verdeyen JT, "Laser Electronics (3rd Edition)," Prentice Hall, Chapter 11, (1995)

[24] Buckman AB, "Guided Wave Photonics," Oxford University Press, Chapter 8, (1995)

[25] Lee, Tien-Pei, Burrus Jr, Charles A, Miller BI, "Stripe-Geometry Double-Heterostructure Ampified-Spontaneous-Emission (Superluminescent) Diode," *IEEE Journal of Quantum Electronics*, QE-9.8 (1973) 820-828

[26] Huber R, Wojtkowski M, Taira K, Fujimoto J, Hsu K, "Amplified, Frequency Swept Lasers for Frequency Domain Reflectometery and OCT Imaging - Design and Scaling Principles," *Optics Express*, 13.9 (2005) 3513-3528

[27] Larina I, Larin K, Justice M, Dickinson M, "Optical Coherence Tomography for Live Imaging of Mammalian Development," *Current Opinion in Genetics and Development*, 21.5 (2011) 579-584

[28] Bouma BE, Yun SH, Vakoc BJ, Suter MJ, Tearney GJ, "Fourier-Domain Optical Coherence Tomography - Recent Advances Toward Clinical Utility," *Current Opinion in Biotechnology*, 20.1 (2009) 111-118

[29] Davis AM, Choma MA, Izatt JA, "Heterodyne Swept-Source Optical Coherence Tomography for Complete Complex Conjugate Ambiguity Removal," *Journal of Biomedical Optics*, 10.6 (2005) 064005

[30] Vakhtin AB, Kane DJ, Wood WR, Peterson KA, "Common-Path Interferometer for Frequency-Domain Optical Coherence Tomography," *Applied Optics*, 42.34 (2003) 6953-6958

[31] Sharma U, Kang JU, "Common-Path Optical Coherence Tomography with Side-Viewing Bare Fiber Probe for Endoscopic Optical Coherence Tomography," *Review of Scientific Instruments*, 78.11 (2007) 113102

[32] Wojtkowski M, Grulkowski I, Szkulmowska A, Szkulmowski M, Bajraszewski T, Targowski P, Kowalczyk A, "Real-Time In-Vivo Ophthalmic Imaging by Ultra Fast Spectral Optical Coherence Tomography," *Proceedings of SPIE - Coherence Domain Optical Methods*, 4956.1 (2010) 50-54

[33] O'Donnell AT, Kim CC, "Update and Clinical Use of Imaging Technologies for Pigmented Lesions of the Skin," *Seminars in Cutaneous Medicine and Surgery*, 31.31 (2012) 38-44

[34] Gambichler T, Regeniter P, Bechara FG, Orlikov A, Vasa R, Moussa G, Stucker M, Altmeyer P, Hoffmann K, "Characterization of Benign and Malignant Melanocytic Skin Lesions Using Optical Coherence Tomography In-Vivo," *Journal of the American Academy of Dermatology*, 57.4 (2007) 629-637

[35] Su J, Zhang J, Yu L, Colt HG, Brenner M, Chen Z, "Real-Time Swept Source Optical Coherence Tomography Imaging of the Human Airway Using a Microelectromechanical System Endoscope and Digital Signal Processor," *Journal of Biomedical Optics Letters*, 13.3 (2008) 030506

[36] Alder DC, Zhou C, Tsai TH, Schmitt J, Hugang Q, Mashimo H, Fujimoto JG, "Three-Dimensional Endomicroscopy of the Human Colon Using Optical Coherence Tomography," *Optics Express*, 17.2 (2009)

[37] Zhong S, Shen YC, Ho L, May RK, Zeitler JA, Evans M, Taday PF, Pepper M, Rades T, Gordon KC, Muller R, Kleinebudde P, "Non-Destructive Quantification of Pharmaceutical Tablet Coatings Using Terahertz Pulsed Imaging and Optical Coherence Tomogrpahy," *Optics and Lasers in Engineering*, 49.3 (2011) 361-365

[38] Haskell RC, Liao D, Pivonka AE, Bell TL, Haberie BR, Hoeling BM, Petersen DC, "Role of Beat Noise in Limiting the Sensitivity of Optical Coherence Tomography," *Journal of the Optical Society of America A*, 23.11 (2006) 2747-2755

[39] Li X, Han JH, Liu X, Kang JU, "Signal-to-Noise Ratio Analysis of All-Fiber Common-Path Optical Coherence Tomography," *Applied Optics*, 47.27 (2008) 4833-4840

[40] Tan KM, Mazilu M, Chow TH, Lee WM, Taguchi LK, Ng BK, Sibbett W, Herrington CS, Brow CTA, Dholakia K, "In-Fiber Common-Path Optical Coherence Tomography Using a Conical-Tip Fiber," *Optics Express*, 17.4 (2009) 2375-2384

[41] Huang W, Day DE, Kittiratanapiboon K, Rahaman MN, "Kinetics and Mechanisms of the Conversion of Silicate (45S5), Borate, and Borosilicate Glasses to Hydroxyapatite in Dilute Phosphate Solutions," *Journal of Materials Science - Materials in Medicine*, 17.7 (2006) 583-596

[42] Yao A, Wang D, Huang W, Fu Q, Rahaman MN, Day DE, "In-Vitro Bioactive Characteristics of Borate-Based Glasses with Controllable Degredation Behavior," *Journal of the American Ceramic Society*, 90.1 (2007) 303-306

[43] Fu H, Fu Q, Zhou N, Huang W, Rahaman MN, Wang D, Liu X, "In-Vitro Evaluation of Borate-Based Bioactive Glass Scaffolds Prepared by a Polymer Foam Replication Method," *Materials Science and Engineering C*, 29.7 (2009) 2275-2281

VITA

Edward Henry Pienkowski Jr. was born on August 10, 1984 in St. Louis, MO. In May 2007, he received his bachelor's degree. in Biomedical Engineering from Saint Louis University, St. Louis, MO.

In June 2010, he enrolled at the Missouri University of Science and Technology in order to pursue a master's degree in Electrical Engineering under the guidance of Dr. Hai Xiao. The focus of Edward's studies was photonic medical imaging systems and their applications. In May 2012, he received his Master of Science Degree in Electrical Engineering from the Missouri University of Science and Technology, Rolla, Missouri, USA.